Three-dimensional effects on the dynamic fracture determination of Al 7075-T651 using TPB specimens

J.A. Loya *, J. Fernández-Sáez

Department of Continuum Mechanics and Structural Analysis, University Carlos III of Madrid, Avda. de la Universidad 30, 28911, Leganés, Madrid, Spain

Abstract

Here we present a numerical analysis of three dimensional effects on the dynamic three point bending fracture tests on Al 7075 T651 alloy specimens performed in a modified Split Hopkinson Pressure Bar. Using the Finite Element Method implemented in a commercial code the whole experimental device has been modeled. Different thicknesses and initial crack to width ratio specimens are simulated at different impact velocities to study the possible effect on the Crack Mouth Open ing Displacement and, using a local stress fracture criterion, in the critical Stress Intensity Factor. The numerical results are compared with experimental results found by the authors.

PACS: 01.30. y

Keywords: Dynamic three point bending test; Dynamic fracture; Numerical simulation

1. Introduction

The knowledge of dynamic fracture behaviour of materials at high strain rates is required to design components subjected to dynamic loads. In mode I, this behaviour is described by fracture parameters such as the dynamic fracture-initiation toughness, K_{Id}, which represents the value of the Stress Intensity Factor, SIF, at which a crack begins to propagate.

The methodology for the determination of the dynamic fracture-initiation toughness, K_{Id}, is not standardized as in the static conditions, K_{IC}, and thus different techniques have been used to evaluate the dynamic fracture properties of materials. One of the most widely used is the instrumented Charpy test, but the maximum loading rate (Stress Intensity Factor loading rate, $\dot{K}_I$) achieved during the test is about $\dot{K}_I = 10^5$ MPa$\sqrt{}$m/s. For higher strain rates, special arrangements of the Split Hopkinson Pressure Bar (SHPB) for dynamic bend-

* Corresponding author. Tel.: +34 916248880; fax: +34 916249973.
E mail addresses: jloya@ing.uc3m.es (J.A. Loya), jloya@ing.uc3m.es (J. Fernández Sáez).
URLs: http://authors.elsevier.com/locate/latex (J.A. Loya), http://authors.elsevier.com/locate/latex (J. Fernández Sáez).

ing tests (Ruiz and Mines, 1985; Yokoyama, 1993; Bacon et al., 1994; Rubio, 1999) have been proposed. The system (see Fig. 1) consists of a striker bar (called projectile or impactor), an input pressure cylinder with a modified shape edge, a supporting device, and the recording equipment. The cracked specimen is placed between the input bar and the supporting device and is loaded to fracture by means of a concentrated transverse force applied at its midspan. The projectile, moving at velocity V_0, strikes the input bar, generating a longitudinal strain compressive pulse, $\varepsilon_i(t)$, that propagates along the bar. This pulse can be recorded by strain gauges on its outer surface. Once the pulse reaches the right edge of the bar, part of its energy is transmitted directly to the specimen and to the supporting device, while the remaining energy is reflected back to the input bar as a tensile pulse, $\varepsilon_t(t)$. The reflected pulse is recorded by the strain gauges. Assuming the theory of one-dimensional elastic wave propagation, the load exerted on the specimen, $P_i(t)$, and the displacement of the edge of the bar initially in contact with the specimen, $u(t)$, can he calculated (Ruiz and Mines, 1985; Yokoyama, 1993; Bacon et al., 1994; Rubio, 1999).

For the experimental determination of K_{Id}, both the time history of the Stress Intensity Factor, $K_{\mathrm{I}}(t)$, during the specimen loading process, and the instant at which the crack in the material begins to grow, t_f, must be determined. Then K_{Id} can be defined as:

$$K_{\mathrm{Id}} = K_{\mathrm{I}}(t_f) \tag{1}$$

Some authors (Kishimoto et al., 1980, 1984) have developed simple formulas for the dynamic SIF on three-point-bending specimens using the Euler Bernouilli (Kishimoto et al., 1980) or Timoshenko (Kishimoto et al., 1984) beam theories, modelling the specimen as a simply supported beam with a crack at its midspan.

Numerical approaches (Yokoyama, 1993; Crouch, 1993) based on the Finite Element Method (FEM) have been used to study the problem. In dynamic tests, the SIF can he evaluated experimentally throughout different optical (Beinert and Kalthoff, 1981; Ravi-Chandar and Knauss, 1984; Benitez and Andrade, 1997) and photoelastic (Dally and Barker, 1988) techniques, but in general they require complex equipment. However, recent two-dimensional numerical analysis of the dynamic three-point-bending test (Rubio et al., 2003), accounting for the possible loss of contact between the interacting bodies, showed that the dynamic SIF can he evaluated with high precision from the measurement of Crack Mouth Opening Displacement, CMOD, throughout the test, assuming that the same relationships between SIF and CMOD used in the static cases apply to the dynamic ones. In this last work (Rubio et al., 2003) a high-speed photography system was used to measure the CMOD directly on the specimen. Popelar et al. (2000) proposed a dynamic test method in which the CMOD was measured by means of a gauge. The aforementioned analyses are based on beam theory and 2D FEM solutions and less information on 3D analysis is found in the literature, but several studies have considered that three-dimensional effects in the determination of fracture properties (Rosakis and Ravi-Chandar, 1986; Narashiman and Rosakis, 1990) may be underestimated in 2D analysis (Loya et al., 2003).

Here we present a numerical analysis of three-dimensional effects on the dynamic three-point-bending fracture tests on Al 7075-T651 alloy specimens performed in a modified Split Hopkinson Pressure Bar. Using the

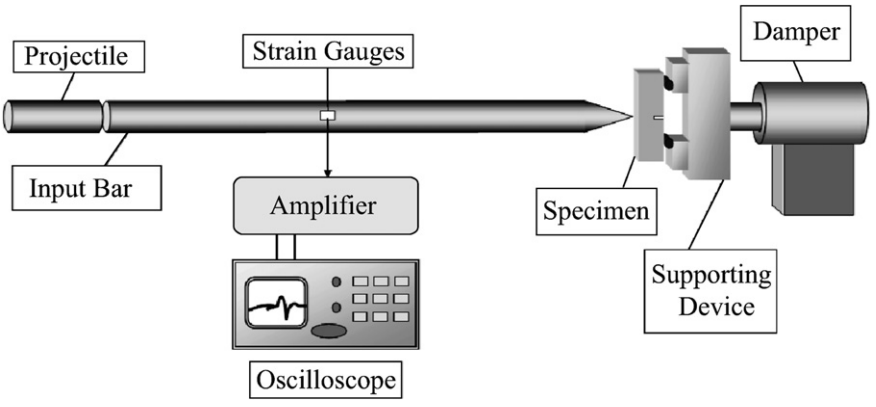

Fig. 1. Modified split Hopkinson Pressure Bar scheme.

Finite Element Method implemented in the commercial code ABAQUS (2003) the whole experimental device has been modeled. Different specimen thicknesses and initial crack-to-width ratio specimens are simulated at several impact velocities to study the effect of these parameters on the CMOD and, using a local stress fracture criterion, in the critical SIF. These effects on the CMOD and critical SIF are compared with experimental results found by the authors (Loya, 2004; Loya and Fernández-Sáez, 2007).

2. Numerical model

A three-dimensional numerical simulation of the impact bending fracture test in a modified Split Hopkinson Pressure Bar was performed by the Finite Element Method using the commercial code ABAQUS (2003). This code uses the Hilber Hughes Taylor direct integration method (Hilber et al., 1978), an implicit and unconditionally stable method for linear systems.

2.1. Geometry

The finite element model includes the whole experimental device, that is, the projectile, the input bar, the specimen and the supporting device. The simulated projectile and input bar were both cylindrical and 22 mm in diameter, and 330 mm and 1000 mm length, respectively. The input bar edge in contact with the specimen presented a modified shape similar to the nose of the Charpy hammer, as is sketched in Fig. 2.

The geometry and dimensions of the specimens, given in Fig. 3, are based on the recommendations of the E1820-01 (2005). For comparison with experimental results previously presented by Loya (2004) and Loya and Fernández-Sáez (2007), its dimensions were: width $W = 20$ mm, span $S = 80$ mm, and total length, $L = 100$ mm. Three-dimensional effects were studied on varying the thickness, B, ($B = 2$ mm, $B = 5$ mm *and* $B = 10$ mm) and the initial crack length, a ($a/W = 0.3$, $a/W = 0.5$, *and* $a/W = 0.7$).

Due to the symmetry in geometry and boundary conditions, only one quarter of the input bar, projectile and specimen, as well as half of one roller support were modelled, reducing the computation cost.

2.2. 3D FEM meshes

The projectile (see Fig. 4) was modeled as a 1/4 of cylinder using 8 nodes hexaedric elements, type $C3D8$, resulting 870 nodes and 550 elements. A similar mesh was used for the input bar (3020 nodes and 1988 elements, type $C3D8$), with the particular shape at the tip of the bar that strikes the specimen, as can be seen in Fig. 5.

The compression pulse generated when the projectile impacts on the input bar, requires that both meshes be refined lengthwise in the direction of the contact surfaces for accurate description, as can be appreciated in Fig. 6.

For the study of the effect of the specimen thickness and crack-to-width ratio, several specimen meshes were used (7303 7744 nodes and 5982 6174 elements, type $C3D8$). Fig. 7 shows the front and side view of the particular case of $(a/W) = 0.5$ and $B = 10$ mm, and the tip of the input bar and the supporting device can also be appreciated.

With close regard to the specimen, this mesh was divided into zones that need special refinement to take into account the stress and strain concentrations (see Fig. 8), such as near the crack tip (detailed at Fig. 9)

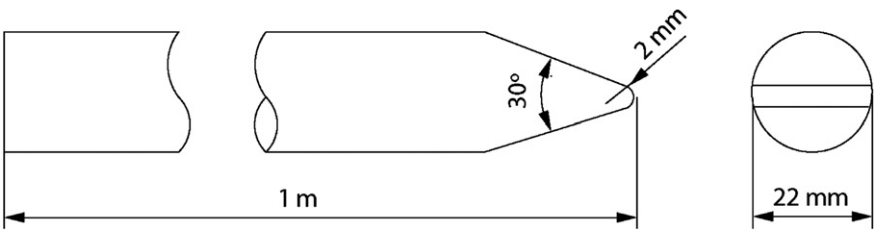

Fig. 2. Input bar scheme.

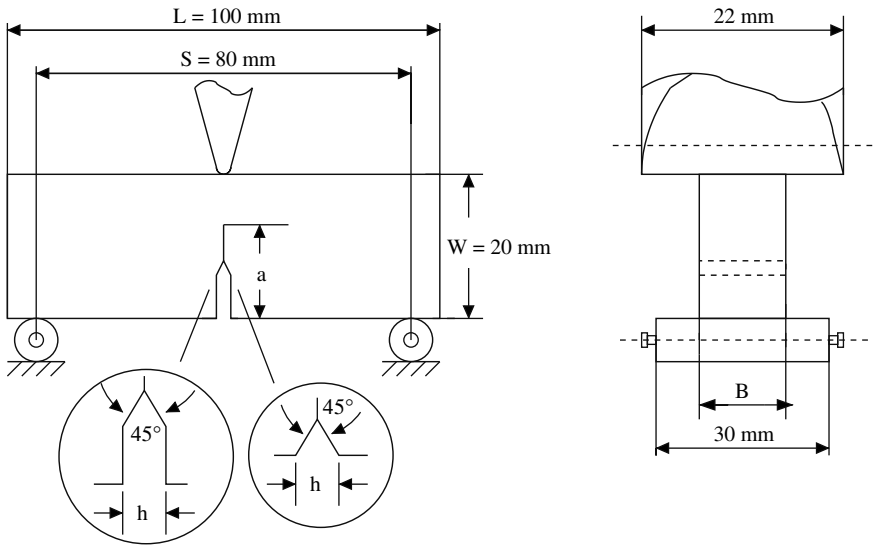

Fig. 3. Bending specimen scheme.

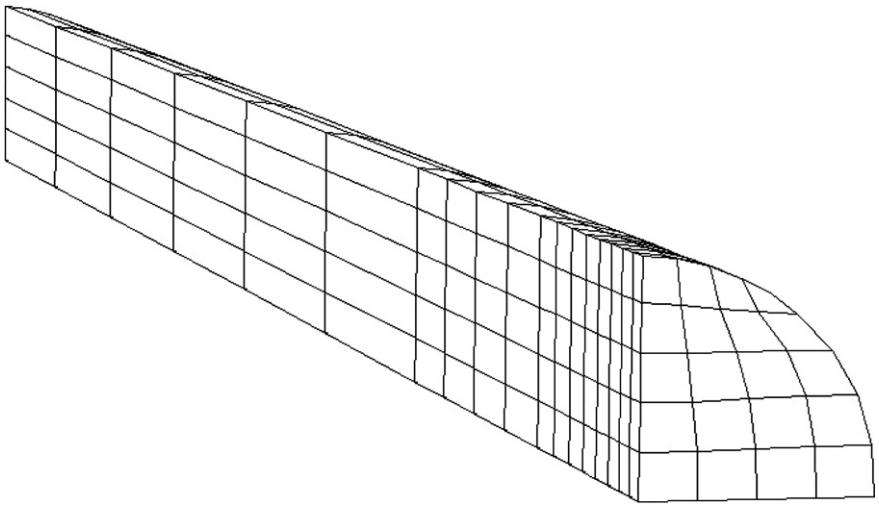

Fig. 4. FEM mesh of the projectile.

and at contact zones between elements (input bar-specimen, specimen-supporting device) to allow possible loss of contact (Fig. 10).

The crack tip zone (Fig. 9) consists of a converging radial shape (25 radial layers), where the smallest element size at the crack tip (6 nodes elements, type *C3D6*) is about 2.8 μm (Fig. 9(a)) and an adaptation mesh (Fig. 9(b)). These refined zones were made by a FORTRAN code to ensure their being exactly the same for the different crack length specimen meshes considered, in an effort to avoid mesh dependency and to compare the results for the simulation of different specimens. For the stress and strain variation to be considered through the specimen thickness, eight element layers were used in the specimen model. From the symmetry plane, $z = 0$, to the free surface, $B/2$, the position of these layers were:

$$\frac{z}{B/2} = \{0,\ 0.26,\ 0.45,\ 0.61,\ 0.74,\ 0.85,\ 0.93,\ 0.98,\ 1\}$$

The supporting device (see Fig. 11) was modeled by a ha1f-cylinder of 8 mm in diameter. To simulate the rest of the support, 60 special elements called''infinite elements'' (*CIN3D8*) provided by ABAQUS (2003) finite ele-

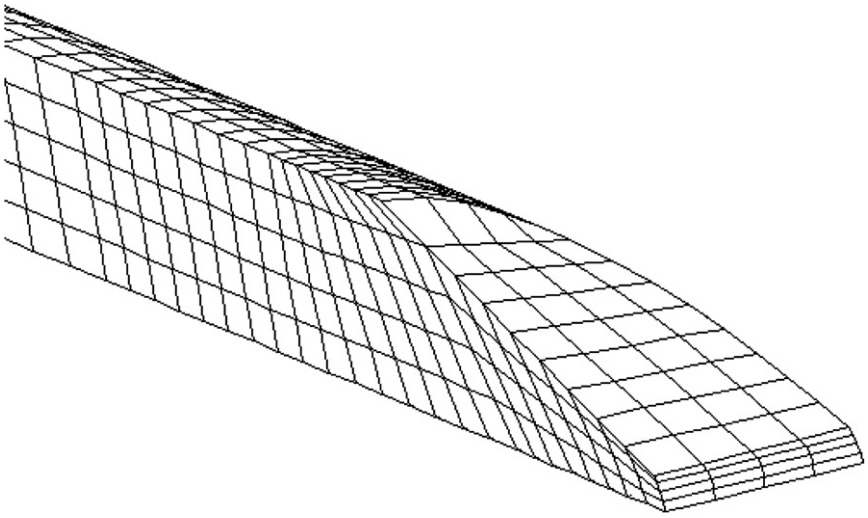

Fig. 5. FEM mesh of the input bar.

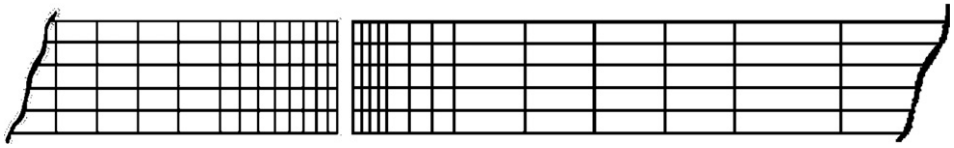

Fig. 6. Detail of the contact projectile input bar.

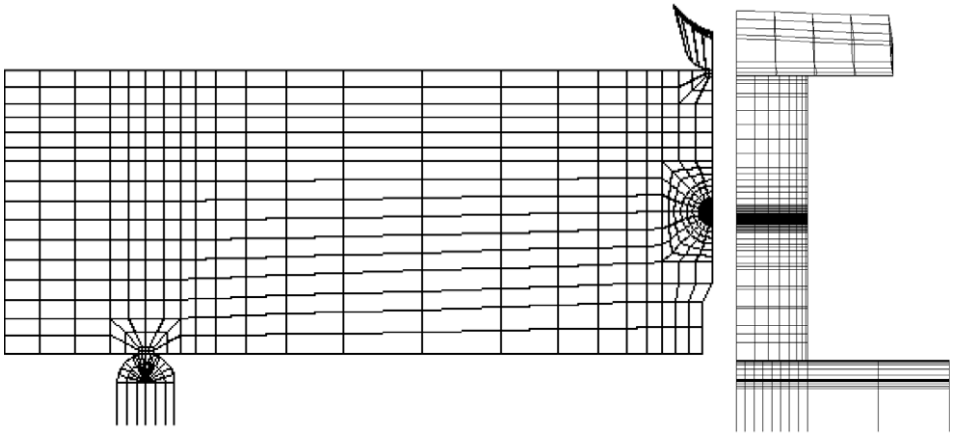

Fig. 7. Front and side view of a one quarter 3D finite element $B = 10$ mm, $(a/W) = 0.5$ specimen mesh.

ment package were used. This kind of element is often used in boundary-value problems defined in unbounded domains, or for problems in which the region of interest is small (specimen) as compared to the surrounding medium (supporting device). These last elements can be used in conjunction with conventional finite elements.

In this dynamic analysis, the infinity elements were chosen for their ability to transmit energy outside the finite element mesh, without trapping or reflecting it. This transmission is optimized when the boundary between finite and infinite elements is orthogonal to the direction from which the waves impinge on this boundary, as in meshes considered.

The total number of nodes and elements of the three-dimensional model of the dynamic tests considered, are described in Table 1.

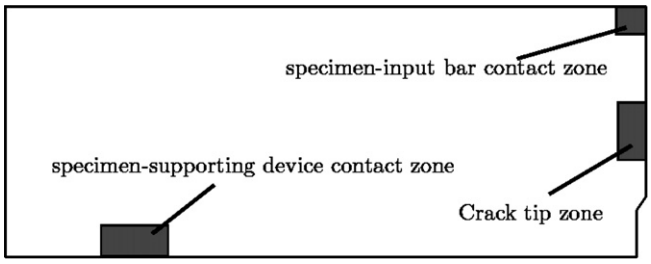

Fig. 8. Special refinement zones in the specimen model.

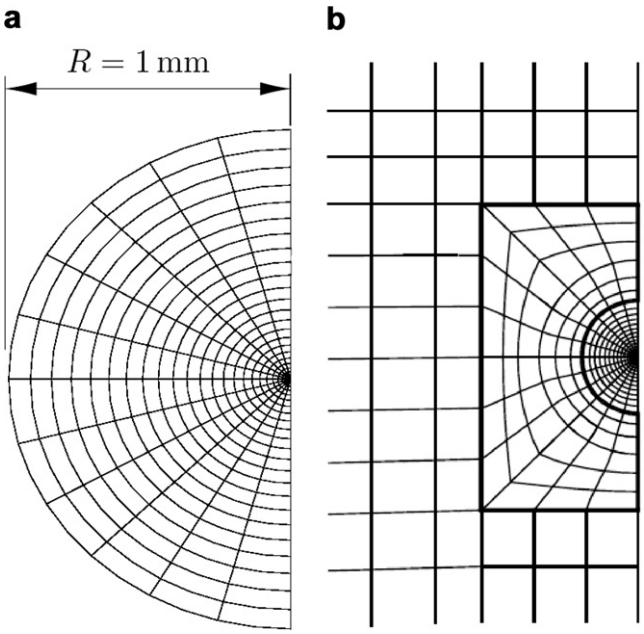

Fig. 9. Crack tip refinement zone. (a) Crack tip zone. (b) Adaptation zone.

To consider strain rate effect, a static analysis was performed by applying an imposed displacement at nodes of the specimen in contact with the input bar. The dynamic cases solved correspond to a projectile impact velocity of 5 m/s and 10 m/s. In this model, no crack growth was considered during the test.

2.3. Material properties

The uniaxial experiments presented under static and dynamic conditions by Loya (2004) are used for the constitutive characterization of the material considered. A linear elastic behaviour was assumed for the projectile, input bar and support material with the following properties: Young modulus $E = 200$ GPa and Poisson coefficient $v = 0.3$. The mass density of this material was $\rho = 7850\ \mathrm{kg/m^3}$.

An elastic viscoplastic behaviour was considered for the specimen material (7075-T651 aluminium alloy) at the contact zone with the input bar and supporting device, and at the crack tip zone, where the elastic properties are: Young modulus $E = 72$ GPa and Poisson ratio $v = 0.3$, and the viscoplastic behaviour used corresponds to a Bodner Partom law:

$$\sigma = \sigma_0(\varepsilon^{\mathrm{pl}}) \cdot \left(1 + \frac{\dot{\varepsilon}^{\mathrm{pl}}}{D}\right)^{\frac{1}{m}} \tag{2}$$

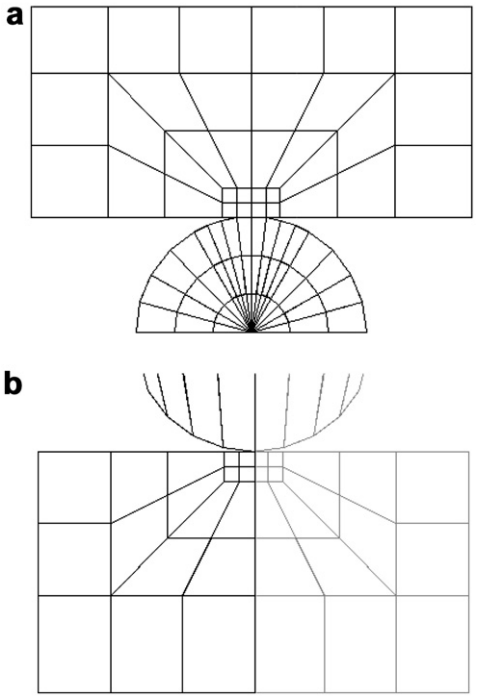

Fig. 10. Refinement details at contact zones. (a) Specimen supporting device. (b) Specimen input bar.

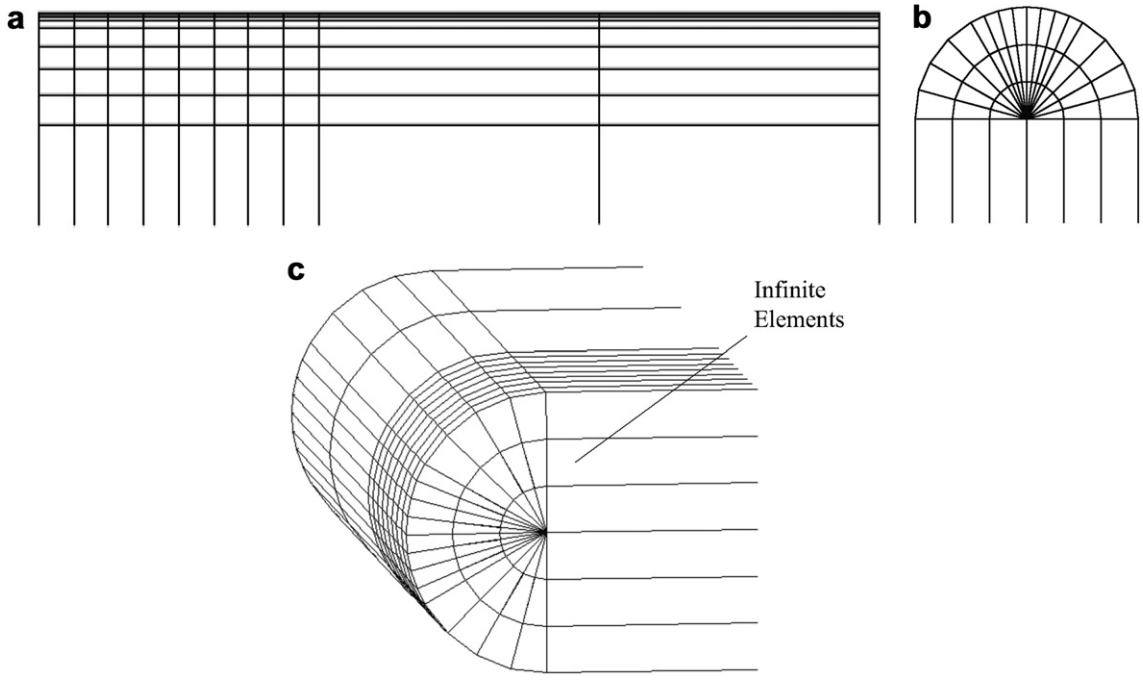

Fig. 11. Supporting device FEM mesh. (a) Upper view. (b) Side view. (c) Perspective view.

where ε^{pl} is the equivalent plastic strain and $\dot{\varepsilon}^{pl}$ the equivalent plastic strain rate. The values of the parameters D and m were $D = 9164$ and $m = 0.93$. The dependence of σ_0 on ε^{pl} was computed as: $\sigma_0(\varepsilon^{pl}) = \sigma_y + k \cdot (\varepsilon^{pl})^n$,

Table 1
Number of nodes and elements in the 3D numerical model

3D model	Projectile	Input bar	Specimen	Supporting device	Total
Nodes	809	320	7303 7744	747	9179 9620
Elements	519	1988	5982 6174	540	9029 9221

with $\sigma_y = 500$ MPa, $k = 673.66$ MPa and $n = 0.0563$ (Loya, 2004). The mass density of this material was $\rho = 2800\ \mathrm{kg/m^3}$.

2.4. Stress intensity factor calculation

Experimentally, the SIF can be determined by different methods. Some authors (Rubio et al., 2003; Loya and Fernández-Sáez, 2007) consider the optimum technique for determining the SIF is through the measurement of the relative displacement of points at the crack mouth, CMOD, applying the well-known relationship as in static conditions.

Consequently, by this method, considering plane strain conditions and assuming that the relationship for the static case applies to the dynamic one (Nishioka and Atluri, 1982), the SIF at the symmetry plane of the specimen can be computed from the CMOD as:

$$K_{\mathrm{I}}(t) = \frac{E \cdot \mathrm{CMOD}}{4\sqrt{a\alpha}} \frac{\kappa_\beta(\alpha)}{\upsilon_\beta(\alpha)} \tag{3}$$

where β is the span-to-width ratio, α is the crack-to-width ratio, and $\kappa_\beta(\alpha)$ and $\upsilon_\beta(\alpha)$ are non-dimensional functions depending on α and β values that can be found in Guinea et al. (1998). For the geometry considered in the present work, where $\beta = 4$, these functions are

$$\kappa_\beta = \frac{\sqrt{\alpha}}{(1-\alpha)^{3/2}(1+3\alpha)}(1.9 + 0.41\alpha + 0.51\alpha^2 - 0.17\alpha^3) \tag{4}$$

$$\upsilon_\alpha = 0.76 - 2.28\alpha + 3.87\alpha^2 - 2.04\alpha^3 + \frac{0.66}{(1-\alpha)^2} \tag{5}$$

2.5. Local stress fracture criterion

The value of the SIF reached when the crack begins to propagate, is the critical SIF, K_c^*. For this instant to be calculated, the time to fracture, t_f, requires the application of a fracture criterion.

Ritchie et al. (1973) presented a local stress fracture criterion (RKR criterion) to explain crack propagation for a two-dimensional problem under static conditions, and was further applied under dynamic conditions by other authors (Wall, 2002; Jayadevan et al., 2002). This criterion holds that a crack propagates when the normal stress to the crack plane, σ_{yy}, at a characteristic distance from the tip of the crack, d_c, reaches a critical value, σ_f (Fig. 12).

In our case, for the estimation of the time to fracture in a 3D problem, a similar consideration was applied at different planes $z =$ constant through the thickness of the specimen (Fig. 13), considering that the crack propagates when the critical conditions are reached at any layer.

Fig. 14 represents the evolution of the stress $\sigma_{yy}(t)$ for elements at an arbitrary distance d_c from the tip of the crack in different layers in the specimen thickness. At any particular time, we find that the stress calculated in these elements is greater as the layer considered is closer to the symmetry plane of the specimen normal to the plane that contains the crack ($z = 0$). Therefore, this plane determines the time to fracture, t_f, and the onset of crack propagation.

Our hypothesis, stated that the critical stress and the critical distance depend only on the material and are strain rate independent (Wall, 2002), so that the parameters of the criterion were determined from the numerical simulation of a particular case, $B = 10$ mm and $(a/W) = 0.5$ under static conditions, and fixed for the dif-

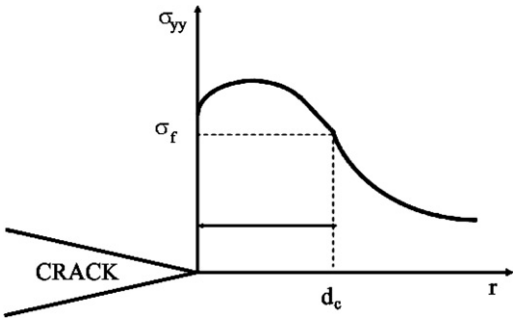

Fig. 12. RKR local fracture criterion.

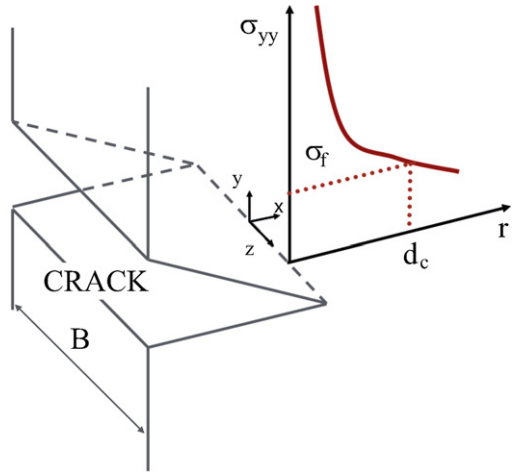

Fig. 13. Local fracture criterion for a plane z constant.

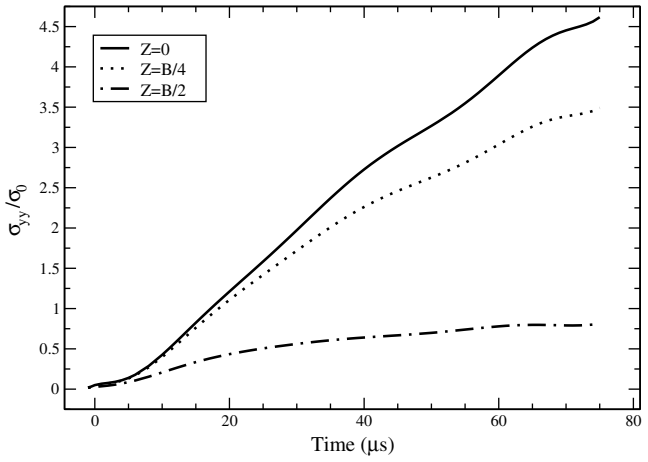

Fig. 14. Evolution of $\sigma_{yy}(t)/\sigma_0$ at different layers through the thickness.

ferent cases considered. For this case, when the numeric SIF reach the experimental value $K_{IC} = 24\ \text{MPa}\sqrt{\text{m}}$, the stress field at $z = 0$ was analyzed and σ_f and d_c can be determined (Loya, 2004). Some authors (Wall, 2002) have confined the critical stress value, σ_f, to the range between $(1.5 - 3)\sigma_y$. In this work, the critical stress was fixed at $\sigma_f = 1.5\ \text{GPa}$ (corresponding to $\sigma_f = 1.5\sigma_y$), which is reached at a critical distance

$d_c = 25$ μm. Naturally, different pairs of d_c and σ_f values can be chosen but the effect in the results is very similar (Wall, 2002).

3. Experimental technique

The experimental technique referred in this work has been detailed in Rubio et al. (2003), Loya (2004) and Loya and Fernández-Sáez (2007), but some brief ideas about stated below.

The critical SIF on TPB specimens was obtained in a modified Split Hopkinson Pressure Bar from the CMOD, recorded by a high-speed photographic device and related with the SIF using the well-known static relationship, that can be applied to the dynamic case.

The time to fracture when the crack begins to propagate was measured by crack propagation gauges in the specimen, which wires breaks as the crack grows. At this moment, the critical CMOD is obtained and the critical SIF calculated.

4. Numerical results and comparison with experiments

From the corresponding numerical simulations of the tests described above, different results can be achieved. Some, such as the traveling waves across the input bar, or the effect in the CMOD history and in the K_c^* of the specimen thickness, crack-to-width ratio or impact velocity, can be compared with those experimentally obtained for the proposed material Al 7075-T651 (Loya, 2004; Loya and Fernández-Sáez, 2007).

4.1. Incident and reflected waves

First of all, Fig. 15 shows the incident and reflected waves registered in a strain gauge located at the mid-length of the input bar during a non-specimen test and the corresponding numerical prediction. This validation is useful to check the quality of the element size and the integration time, resulting in good agreement in the comparison.

4.2. Crack mouth opening displacement

As shown in Fig. 14, the critical fracture properties are reached first at the symmetry plane, but, using the experimental technique described, the CMOD is measured at the free surface of the specimen. Therefore, it is helpful to analyze the variation of the CMOD at different planes of the thickness respect to the symmetry

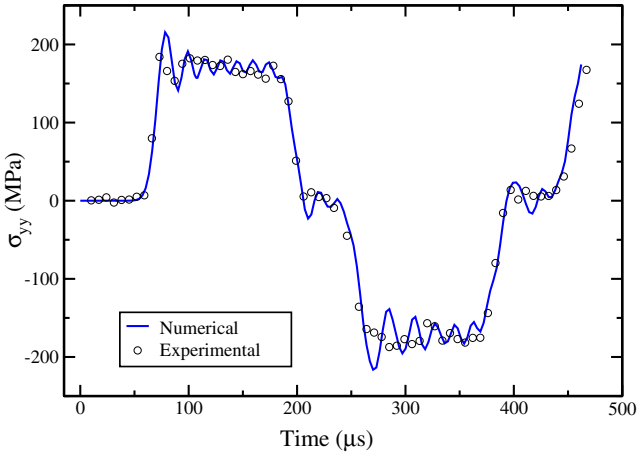

Fig. 15. Incident and reflected waves.

plane, $\Delta CMOD(z)$ (see Eq. (6)). In all cases this variation is lower than 0.15%, and thus the CMOD can be considered constant throughout the thickness (Fig. 16).

$$\Delta CMOD(z) = \frac{CMOD(z) - CMOD(0)}{CMOD(0)} \times 100 \tag{6}$$

Fig. 17 shows the time evolution of CMOD for specimens with the same thickness ($B = 2$ mm) but different crack-to-width ratios, impacted at $V_0 = 10$ m/s. It is appreciable that the compliance of the specimen increases as the initial crack is higher. This effect is similar for any specimen thickness considered.

The effect of the specimen thickness in the CMOD time history is presented in Figs. 18 20. Theses figures show the evolution of the CMOD on specimens with the same crack-to-width ratio ($a/W = 0.3,\ 0.5$ and 0.7, respectively) and three different thicknesses, impacted at $V_0 = 10$ m/s. In these figures, for any particular time considered, it can be seen that the CMOD values are lower as the thickness is bigger. This influence of the thickness can not be observed using a bi-dimensional numerical analysis of the problem.

Once the CMOD history is calculated and the time to fracture, t_f, determined applying the presented local stress fracture criterion, the critical SIF, K_c^*, can be related to the CMOD at the time to fracture ($CMOD(t_f)$) by means of Eq. (3).

Figs. 21 24 present the numerical prediction of the CMOD time history for two different thickness, B 5 and 10 mm, and impact velocity 5 m/s (Figs. 21 and 22) and 10 m/s (Figs. 23 and 24), compared with the cor-

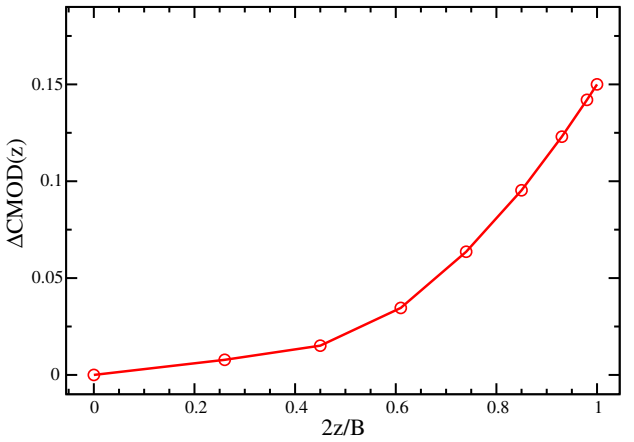

Fig. 16. $\Delta CMOD(z)$ for $B = 10$ mm, $(a/W) = 0.5$ and V_0 10 m/s.

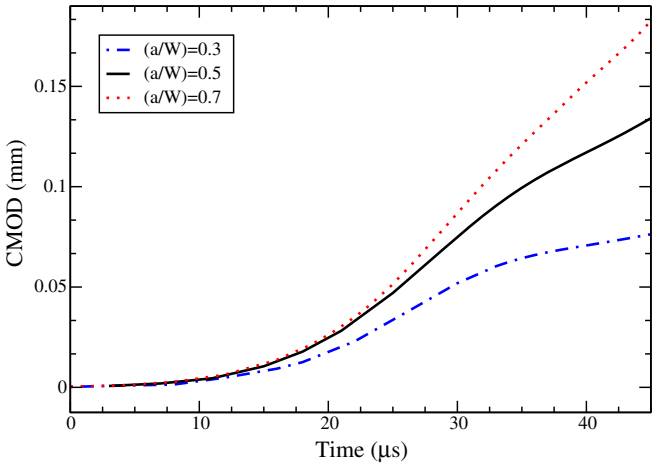

Fig. 17. Evolution of CMOD for $B = 2$ mm and different crack lengths specimens, impacted at V_0 10 m/s.

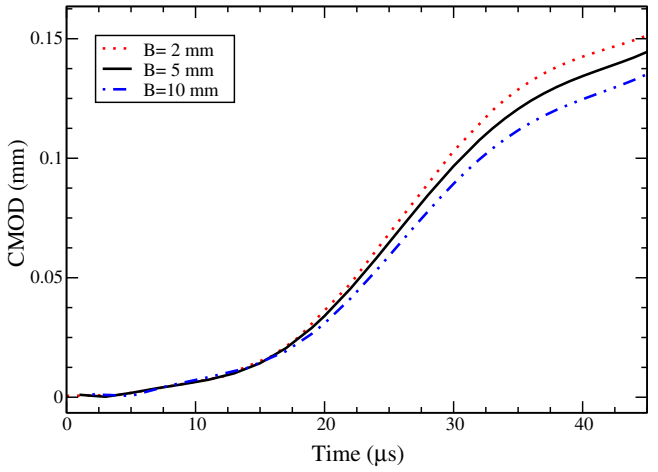

Fig. 18. Evolution of CMOD for (a/W) 0.3 and different thicknesses specimens, impacted at V_0 10 m/s.

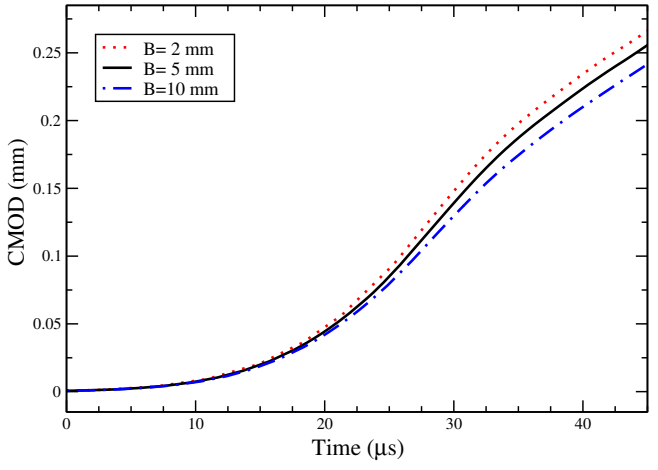

Fig. 19. Evolution of CMOD for (a/W) 0.5 and different thicknesses specimens, impacted at V_0 10 m/s.

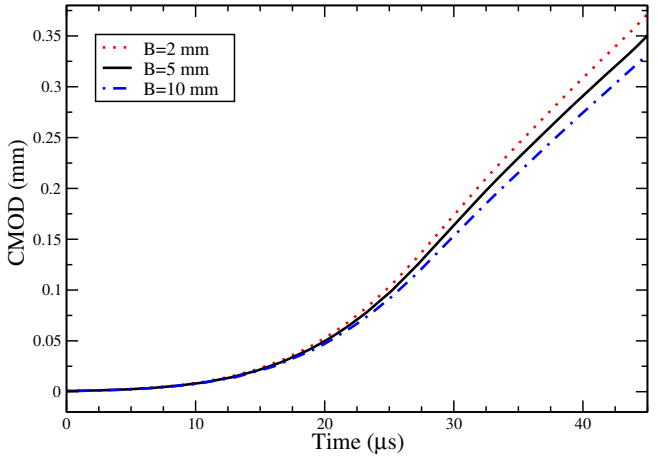

Fig. 20. Evolution of CMOD for (a/W) 0.7 and different thicknesses specimens, impacted at V_0 10 m/s.

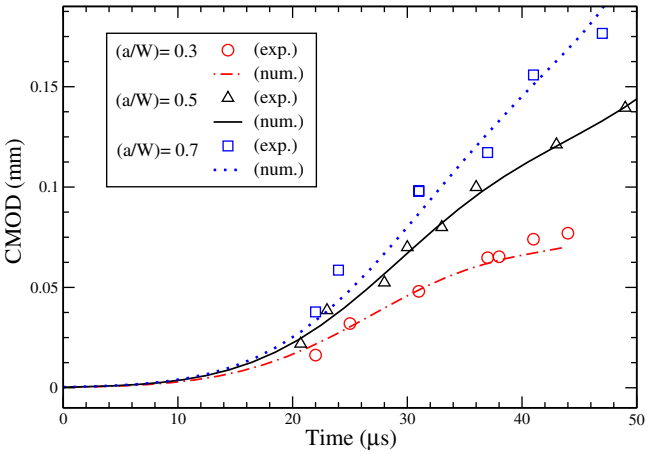

Fig. 21. CMOD history for $B = 5$ mm and V_0 5 m/s.

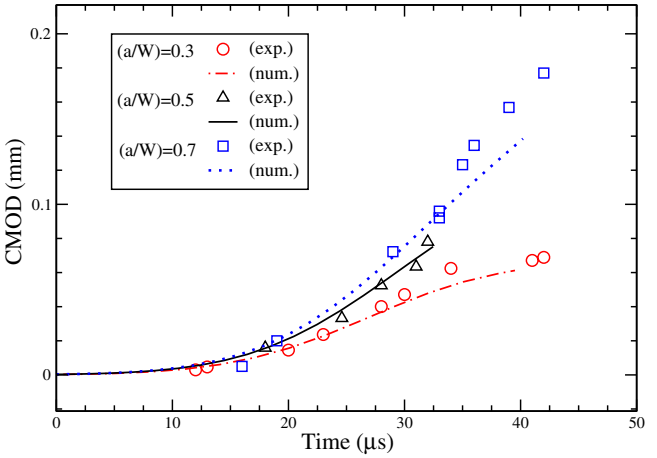

Fig. 22. CMOD history for $B = 10$ mm and V_0 5 m/s.

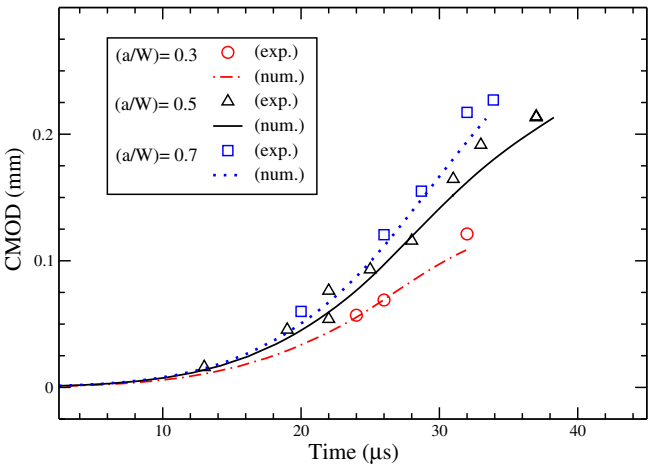

Fig. 23. CMOD history for $B = 5$ mm and V_0 10 m/s.

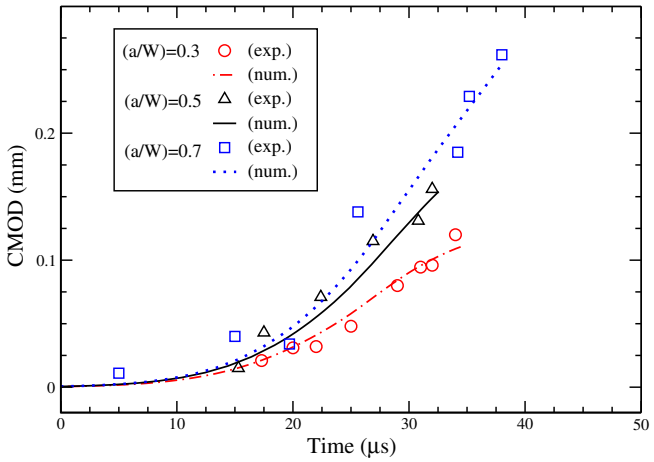

Fig. 24. CMOD history for $B = 10$ mm and V_0 10 m/s.

responding experimental values obtained for a particular specimen (Loya, 2004; Loya and Fernández-Sáez, 2007). The results are presented up to the experimental time to fracture, t_f. These pictures show good agreement between numerical and experimental results, validating the numerical model used.

4.3. Critical stress intensity factor

From the evolution of CMOD determined in the numerical simulations, and from the application of the local stress criterion described above, the critical SIF is calculated.

The numerical values of K_c^* for the specimen thicknesses B 5 mm and 10 mm, and crack-to-width ratio a/W 0.3, 0.5 and 0.7, obtained when the local stress fracture criterion is accomplished, and the corresponding experimental results, are presented for comparison in the Table 2 for static and dynamic conditions and in Tables 3 and 4 for $V_0 = 5$ m/s and $V_0 = 10$ m/s, respectively.

Table 2
Numerical and experimental values of K_c^* and t_f in static conditions

B (mm) Num.	(a/W) Exp.	K_c^*	(MPa$\sqrt{}$m)
5	0.3	26.6	31.2 ± 0.8
5	0.5	24.6	26.0 ± 0.7
5	0.7	23.4	24.0 ± 0.9
10	0.3	26.3	24.6 ± 0.1
10	0.5	24.2	24.2 ± 0.2
10	0.7	23.0	23.3 ± 0.5

Table 3
Numerical and experimental values of K_c^* and t_f at V_0 5 m/s

B (mm)	(a/W)	K_c^* Num.	(MPa$\sqrt{}$m) Exp.	t_f Num.	(μs) Exp.	$\dot{K}_I$ Num.	(10^5 MPa$\sqrt{}$m/s) Exp.
5	0.3	26.3	23.8 ± 3.4	49	44 ± 6	5.3	5.4
5	0.5	24.4	23.6 ± 4.1	45	59 ± 8	5.4	4.0
5	0.7	23.2	22.3 ± 3.8	42	48 ± 6	5.5	4.6
10	0.3	25.8	22.6 ± 3.2	44	42 ± 8	5.9	5.4
10	0.5	23.8	22.2 ± 2.9	34	32 ± 6	7.0	6.9
10	0.7	22.5	21.1 ± 4.1	33	40 ± 7	6.9	5.3

Table 4
Numerical and experimental values of K_c^* ant t_f at V_0 10 m/s

B (mm)	(a/W)	K_c^* Num.	(MPa$\sqrt{}$m) Exp.	t_f Num.	(μs) Exp.	$\dot{K}_I$ Num.	(10^5 MPa$\sqrt{}$m/s) Exp.
5	0.3	25.2	23.7 ± 3.1	29	31 ± 6	8.6	7.6
5	0.5	24.1	23.4 ± 4.2	33	38 ± 5	7.3	6.2
5	0.7	23.0	22.3 ± 3.8	35	33 ± 4	6.4	6.8
10	0.3	24.8	22.5 ± 3.1	31	34 ± 6	8.0	6.6
10	0.5	23.4	21.9 ± 3.1	32	32 ± 7	7.3	6.8
10	0.7	22.2	20.7 ± 4.1	36	38 ± 9	6.1	5.4

Under static conditions, K_c^* decreases as the specimen thickness increases for any crack length. Also, for B constant, K_c^* is lower as the initial crack lengthens.

At impact velocities $V_0 = 5$ m/s and 10 m/s, similar effects can be observed, but the calculated K_c^* values are lower as the impact velocity increases, and the difference due to the crack length is slightly lower.

The comparison reveals that the local stress fracture criterion applied reproduces qualitatively the effect of the thickness, initial crack length and impact velocity in the critical stress intensity factor, which decreases as the thickness, crack-to-width ratio or impact velocity becomes greater. Under static conditions, numerical results are lower than experimental ones, but this tendency is the opposite under dynamic conditions.

Tables 3 and 4 show also the mean SIF loading rate achieved in each test, calculated as $\dot{K}_I = K_c^*/t_f$. As can be seen, the values obtained in all cases were greater than the loading rate that can be obtained by an instrumented Charpy test.

From these results presented, is derived the influence of the impact velocity, V_0, on the $\dot{K}_I$, where the average $\dot{K}_I$ at $V_0 = 10$ m/s is around 35% greater than in at $V_0 = 5$ m/s. About the influence of a/W and B of the $\dot{K}_I$, there are not a clear effect. In general, the K_c^* numerical predictions obtained by means of this simple local fracture criterion match quite well with the experimental values measured in all cases except for the static case $a/W = 0.3$, $B = 5$ mm.

According to the recommendation of the E1820-01 (2005), the specimen thickness, B, must be $B > B_{\min}$, with $B_{\min} = 2.5(K_c^*/\sigma_y)^2$. In our case, $B_{\min}$ is 6 mm. From the numerical and experimental results obtained for K_c^*, probably the stress intensity factor is not adequate for characterization in the cases of thickness lower than $B_{\min}$. Although the recommendation of the E1820-01 (2005) is strictly applicable to static conditions, these results indicate that further effort can be done to analyze the problem for low specimen thickness using other fracture criterion, like the CTOA (Crack Tip Opening Angle), as some investigators have proposed (Kokaly et al., 2001; Dawicke et al., 1995, 1998). Especially, is relevant its application in dynamic conditions, where less information about is found in the literature.

5. Concluding remarks

This work presents a three-dimensional numerical simulation of the dynamic three-point-bending fracture tests performed in a modified Hopkinson Split Pressure Bar using the Finite Element Method implemented in the commercial code ABAQUS.

This 3D model includes the whole experimental device: the projectile, incident bar, specimen, and the supporting device. The dynamic bending simulations include different specimen thickness values (B 2 mm, 5 mm and 10 mm) and different initial crack length values (a/W 0.3, 0.5 and 0.7), and were tested under static conditions and for different impact velocities (5 m/s and 10 m/s). The experimental device material was modeled using perfect elastic steel properties, meanwhile the specimen material (Al 7075-T651) was perfect elastic in the most of the specimen, but elastic viscoplastic behaviour was considered near the crack tip, and close to the interaction zones between the specimen and the input bar and the supporting device.

The CMOD history calculated for the different thicknesses, crack-to-length ratios and impact velocity combinations, were compared with the experimental results with good agreement. The difference between numerical and experimental results increased over the experimental time to fracture, because the numerical model does not consider the crack propagation which occur in the experimental tests.

A local stress criterion was used to determine the instant when the critical fracture conditions are reached. This criterion considers that a crack propagates when a critical stress is reached at a characteristic distance from the crack tip at any layer of the specimen thickness. This condition is reached first at the $z = 0$ layer, corresponding to the symmetry plane of the specimen perpendicular to the plane of the crack, determining the time to fracture. The critical parameters, considered strain rate independent, were identified by a comparison of a particular case (B 10 mm and $(a/W) = 0.5$ in static conditions) with the corresponding experimental test.

The critical SIF, K_c^*, was obtained from the CMOD at t_f, concluding that K_c^* decreases as the thickness or the initial crack length becomes greater, in static and dynamic conditions. In addition, this critical parameter is lower for higher impact velocities, due to the viscoplastic behaviour considered for the specimen modeled.

Thickness and crack length effects agree with the well-known fracture results under static conditions, so that local fracture criterion application seems to be correct to explain these tendencies.

The numerical results presented in this work for dynamic conditions, obtained using a local stress fracture criterion, have been compared to experimental results (Loya, 2004; Loya and Fernández-Sáez, 2007) with a good agreement.

References

ABAQUS, 2003. User's Manual Version 6.4. Hibbitt, Karlsson & Sorensen, Inc.

ASTM E1820 01, 2005. Standard test method for measurement of fracture toughness, Annual book of ASTM standards, vol. 03.01. American Society for Testing and Materials, West Conshohocken, PA.

Bacon, C., Farm, J., Lataillade, J., 1994. Dynamic fracture toughness determined from load point displacement. Experimental Mechanics 20 (1), 217 223.

Beinert, J., Kalthoff, J., 1981. Experimental determination of dynamic stress intensity factors by shadow patterns. In: Sih, G. (Ed.), . In: Mechanics of Fracture, vol. 7. Martinus Nijhoff, La Hague, pp. 281 330.

Benitez, F., Andrade, L., 1997. In plane impact loading of composites: optical evaluation and crack severity assessment for Graphite Epoxy. Journal de Physique IV France 7, C3 169 C3 176.

Crouch, B., 1993. Finite element modeling of the three point bend impact test. Computers and Structures 48 (4), 167 173.

Dally, J., Barker, D., 1988. Dynamic measurements of initiation toughness at high loading rates. Experimental Mechanics 28 (3), 298 303.

Dawicke, D.S., Sutton, M.A., Newman, J., Bigelow, C., 1995. Measurement and analysis of critical CTOA for an aluminum alloy sheet. In: Erdogan, F. (Ed.), Fracture Mechanics, vol. 25. ASTM STP 1296, pp. 358 379.

Dawicke, D., Piascik, R., Newman, J., 1998. Measurement and analysis of critical CTOA for an aluminum alloy sheet. In: Piascik, R., Newman, J., Dowling, N. (Eds.), Fatigue and Fracture Mechanics, vol. 27. ASTM STP 1296, pp. 90 104.

Guinea, G., Pastor, J., Planas, J., Elices, M., 1998. Stress intensity factor compliance and CMOD for a general three point bend beam. International Journal of Fracture 89 (3), 103 116.

Hilber, H., Hughes, T., Taylor, R., 1978. Collocation, dissipation and 'overshoot' for time integration schemes in structural dynamics. Earthquake Engineering and Structural Dynamics 6, 99117.

Jayadevan, K.R., Narasimhan, R., Ramamurthy, T.S., Dattaguru, B., 2002. Effect of t stress and loading rate on crack initiation in rate sensitive plastic materials. International Journal of Solids and Structures 39, 1757 1775.

Kishimoto, K., Aoki, S., Sakata, M., 1980. Simple formula for dynamic stress intensity factor of pre cracked Charpy specimen. Engineering Fracture Mechanics 13 (3), 501 508.

Kishimoto, K., Kuroda, K., Aoki, S., Sakata, M., 1984. Simple formulae for dynamic fracture mechanics parameters of elastic and viscoelastic three point bend specimens based on Timoshenko's beam theory. In: Valluri, S., Taplin, D.M.R., Rama Rao, P., Knott, J.F., Dubey, R. (Eds.), . In: Proceeding of 6th International Conference on Fracture, New Delhi (India), vol. 5. Pergamon, Oxford, pp. 3177 3184.

Kokaly, M., Lee, J., Kobayashi, A.S., 2001. Dynamic ductile fracture of 7075 T6 an experimental analysis. International Journal of Solids and Structures 38, 1935 1942.

Loya, J.A., Fernández Sáez, J., Navarro, C., 2003. Numerical simulation of dynamic TPB fracture test in a modified Hopkinson bar. Journal de Physique IV 110, 305 310.

Loya, J.A., Fernández Sáez, J., 2007. Effect of the thickness, initial crack length and impact velocity on fracture dynamic initiation toughness of aluminum alloy. Journal of Testing and Evaluation 35 (1), 25 30.

Loya, J.A., 2004. Efectos tridimensionales en la determinación de la tenacidad de fractura dinámica. Ph.D. Thesis, University Carlos III of Madrid.

Narashiman, R., Rosakis, A., 1990. Three dimensional effects near a crack tip in a ductile three point bend specimen, Part I: numerical investigations. Journal of Applied Mechanics (2), 121 134.

Nishioka, T., Atluri, S., 1982. A method for determining dynamic stress intensity factors from COD measurement at the notch mouth in dynamic tear testing. Engineering Fracture Mechanics 16 (3), 333 339.

Popelar, C., Anderson Jr., C., Nagy, A., 2000. An experimental method for determining dynamic fracture toughness. Experimental Mechanics 40 (4), 401 407.

Ravi Chandar, K., Knauss, W., 1984. An experimental investigation into dynamic fracture: I crack initiation and arrest.. International Journal of Fracture 25, 247 262.
Ritchie, R.O., Knott, J.F., Rice, J.R., 1973. On the relationship between critical tensile stress and fracture toughness in mild steel. Journal of the Mechanics and Physics of Solids 21, 395 410.
Rosakis, A., Ravi Chandar, K., 1986. On the crack tip stress state: an experimental evaluation of three dimensional effects. International Journal of Solids and Structures 22 (2), 121 134.
Rubio, L., Fernández Sáez, J., Navarro, C., 2003. Determination of dynamic fracture initiation toughness using three point bending tests in a modified Hopkinson pressure bar. Experimental Mechanics 43, 379 386.
Rubio, L., 1999. Determinación de parámetros de fractura dinámica a alta velocidad de deformación. Ph.D. Thesis, University Carlos III of Madrid.
Ruiz, C., Mines, R., 1985. The Hopkinson Pressure Bar: an alternative to the instrumented pendulum for Charpy test. International Journal of Fracture 29 (2), 101 109.
Wall, O., 2002. Numerical modeling of fracture initiation in large steel specimens at impact. Engineering Fracture Mechanics 69, 851 863.
Yokoyama, T., 1993. Determination of dynamic fracture initiation toughness using a novel impact bend test procedure. Journal of Pressure Vessel Technology 115 (2), 389 397.